
ANALYSIS OF FUNCTIONAL NEURAL CODES OF DEEP LEARNING MODELS: FUNCTIONAL TELESCOPE HYPOTHESIS

A PREPRINT

Jung H. Lee
Pacific Northwest National Laboratory
Seattle, WA
jung.lee@pnnl.gov

Sujith Vijayan
School of Neuroscience
Virginia Tech
Blacksburg, VA
neuron99@vt.edu

August 15, 2023

ABSTRACT

Deep neural networks (DNNs), the agents of deep learning (DL), require a massive number of parallel/sequential operations. This makes it difficult to comprehend DNNs' operations and impedes proper diagnosis. Without better knowledge of their internal process, deploying DNNs in high-stakes domains can lead to catastrophic failures. Therefore, to build more reliable DNNs/DL to be deployed in high-stakes real-world problems, it is imperative that we gain insights into DNNs' internal operations underlying their decision-making. Here, we use the self-organizing map (SOM) to analyze DL models' internal codes associated with DNNs' decision-making. Our analyses suggest that shallow layers close to the input layer compress features into condensed space and that deep layers close to the output layer expand feature space. We also found evidence indicating that compressed features may underlie DNNs' vulnerabilities to adversarial perturbations.

1 Introduction

Deep learning (DL) can train artificial agents (deep neural networks, DNNs) with examples to perform a wide range of real-world problems [1, 2, 3], removing the necessity of human experts' instructions. DNNs can even outperform humans in multiple domains, but they depend on a large number of linear, and nonlinear operations, making their operations incomprehensible. Without better understanding their operations, we cannot conduct timely predictions of failures or perform diagnosis, and without proper diagnosis, we cannot safely deploy DNNs in the real world [4, 5]. Furthermore, DL is vulnerable to adversarial perturbations, the imperceptible changes crafted to disrupt DL models' decisions-making [6, 7, 8].

Therefore, to utilize DL's capability in high-stakes domains, it is imperative that we better understand how DNNs make decisions. As DNNs successively transform inputs into final predictions, probing hidden layers' responses can shed light on DNNs' operations. Earlier studies showed that shallow layers (i.e., layers close to the input layer) encode simple low-level features, whereas deep layers (i.e., layers close to the output layer) encode high-level features [9, 10, 11]. The high level features sometimes include human interpretable features. Notably, the low-level features in the shallow layers resemble the features, to which biological neurons in the early stage of visual systems would respond [12].

Then, two important questions arise. How do individual layers evolve? And how do they contribute to DNNs' decisions? Multiple studies have been dedicated to answer these questions, which has led to a subfield of DL named 'explainable AI'. The studies can fall into three categories. The first line of studies estimated the influence of inputs on DNNs' decisions. Specifically, several studies utilized gradient-based analysis [13, 14, 15], layerwise relevance propagation that assigned individual neurons' relevance using backpropagation-like rules [16], and occlusion analysis that measured input patches' influence [10]. The second line of studies focused on analyzing hidden layer representations (HLRs). The feature visualization [17, 11] inverted DNNs to identify optimal features that can drive certain hidden layers. TCAV used examples with and without human-annotated concepts to train a secondary model to learn concept vectors [18].

Once the secondary model is trained, it can evaluate the influence of concept vectors on DL models. Finally, the third line of studies evaluated direct relationships between HLRs and DNNs’ decisions [19, 20].

Here, to better understand the functional codes (FCs) underlying DNNs’ operations, we used unsupervised learning to analyze HLRs. Our study is based on the assumption that the number of FCs is much smaller than the dimension of input feature space, and the mapping between inputs and FCs should be many-to-one. If each input can be mapped onto a unique FC, DNNs can effectively become memory cells that do not generalize thier predictions on unknown inputs (queries). We also assumed that FCs appear repeatedly during DNNs’ operations. With these assumptions in mind, we used the self-organizing map (SOM) [21, 22], an unsupervised learning algorithm, to probe HLRs. Our analyses suggest that shallow layers in DNNs compress feature space, while deep layers expand it, as convex and concave lenses in telescopes collect light and enhance images’ resolution, which we call the functional telescope (FT) hypothesis. We also found evidence suggesting that compressed features may underlie DNNs’ vulnerabilities to adversarial perturbations.

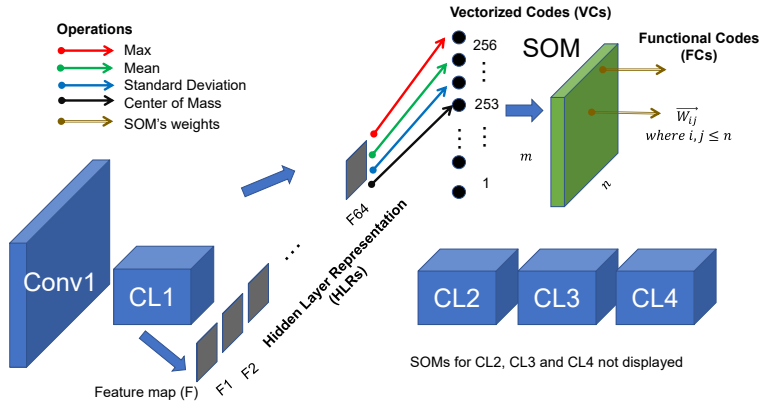


Figure 1: Schematics of SOM-based analysis. We display ResNet18 as an example. The same approach is applied to ResNet50. We convert individual feature maps’ responses to vectorized codes (VCs) using max, mean, standard deviation and center of mass. VCs are abstract representations of feature map outputs (hidden layer representations) and are inputs to a SOM, which identifies functional codes.

2 Approach

In this study, we refer to raw hidden layer outputs as ‘hidden layer representations (HLRs)’, which are known to be highly variable and sensitive to input pixel intensities. We refer to internal representations, which mediate semantic meanings of inputs, as ‘functional codes (FCs)’. To discover FCs used by DL models, we first convert HLRs into more abstract codes by characterizing feature maps’ outputs with their statistical properties.

2.1 Codes of feature maps

Convolution filters produce 2-dimensional outputs (feature maps), which reflect the spatial distribution of inputs. In modern DNNs, the dimension of all features produced by these filters is often too big. If we take activations of all feature maps by flattening them into 1D vectors, the final vectors reflecting individual layers can contain a great amount of stochastic noise, making the analysis overly sensitive to statistical fluctuation or biases that may be irrelevant to semantic information of inputs. Earlier studies employed various dimension reduction algorithms to analyze features; see [23, 24, 25] for example. Specifically, Alain and Bengio [19] used two dimension reduction methods. First, responses were randomly sampled from a subset of spatial locations of feature maps. This ‘random sampling’ was also used by other studies [23, 24]. Second, 2D pooling was used to reduce the number of features to the number of channels. We note that random sampling or naive 2D pooling can result in some crucial information of inputs to be lost, especially in shallow layers, in which feature maps have large spatial dimensions (both height and width). To minimize the loss of information, we coded the individual feature maps by taking max, mean, standard deviation (SD) and center of mass (CM) of activations (Fig. 1), which may help us partially preserve spatial information of the feature maps and make our analysis insensitive to some stochastic/spurious noises independent of inputs’ semantic meanings. These abstract codes will be referred to as vectorized codes (VCs) below.

2.2 Identification of FCs

As VCs from HLRs reflect internal representations of DNNs, we can consider them as FCs, but VCs can also be sensitive to input noises. Thus, we sought representative VCs as ‘effective’ FCs, which can be more directly linked to DNNs’ decision-making. This is based on the assumption that VCs can be decomposed into representative codes and noises, which is inspired by the fact that DNNs perform effective averaging that filters out noises in internal codes via summations/convolutions in their normal operations. Notably, self-organizing map (SOM) [21, 22] can identify representative inputs and their relationships in high dimensional feature space. Thus, we used SOM to identify effective FCs from VCs.

Fig. 1 illustrates our experiment procedure. We first recorded HLRs from hidden layers to obtain VCs and then trained a SOM on VCs to identify FCs. In this study, we used SOMs to analyze two popular ImageNet models, ResNet18 and 50. ResNets consist of 4 composite blocks ([26]), which will be referred to as the composite layer (CL) below (Fig. 1). As 4 CLs (CL1, 2, 3 and 4) represent ResNets’ early, mid and late processing stages, we analyzed HLRs from them. Timm, an open source pytorch library [27], was used to construct the two models pretrained on ImageNet. We obtained HLRs from examples randomly chosen from ImageNet [28]. Then, HLRs were converted to 1-dimensional VCs using max, mean, SD and CM. Following this rule, we obtained 256, 512, 1024, 2048-dimensional VCs from ResNet18; ResNet50’s codes are 4 times bigger due to the number of feature maps.

2.3 SOM and its training to determine FCs

SOM consists of units distributed over 2-dimensional grids [21, 22]. Each unit stores a single weight vector, whose length is the same as that of an input. During training, each input is compared to the weights stored in the units, and the best matching unit (BMU) is identified. Then, the weight of BMU and its neighbors are updated according to the learning rule (Eq. 1).

$$W_v(s+1) = W_v(s) + \exp\left(-\frac{D^2}{2\sigma(s)^2 + \epsilon}\right) \times \alpha(s) \times (x - W_v(s)) \quad (1)$$

, where s denotes training index; u and v denote the best matching unit (BMU) and a unit to be updated, respectively; where W denotes a weight; where α is a learning rate; x is an input; where $D = \|x - W_u\|$, distance metric; ϵ is added for numerical stability.

With this update rule, SOM’s weights move towards the input depending on the location of the units. The weight of BMU moves most strongly, and the weight changes in other units decrease, as their distance to BMU increases. Notably, SOM has two properties. First, the weights of SOM tend to be similar to the inputs and represent exemplary inputs after training. Second, the neighboring units store similar weights, and consequently the distance between BMUs reflects the similarity between the inputs. That is, after training, the similarity between the two inputs can be measured with the distance between their corresponding BMUs. We used these properties to analyze HLRs of ResNets.

We used two sets of 50,000 inputs randomly drawn from ImageNet [28]. The first set (SOM-tr) was built with the ImageNet train set, and the second set (SOM-val), with the ImageNet validation set. Both sets contain 50 examples per each ImageNet class. Only SOM-tr was used to train SOMs, and SOM-val was used to probe their responses to unseen examples. For individual inputs from the two sets, we obtained VCs from 4 CLs of ResNets and grouped them according to layers (i.e., CL). VCs from the same layer were used to train and test a SOM. As there are 4 CLs, we built and trained 4 independent SOMs. A wide range of distance metrics have been used for SOMs in the earlier studies, and we selected the cosine distance (CD, Eq. 2) to measure the similarity between SOMs’ weights and a VC. SOMs were constructed with the periodic boundary to avoid boundary effects observed during training. With the periodic boundary condition, SOM effectively became a 2-dimensional torus, and the distance was measured accordingly.

$$CD(u, v) = 1 - \frac{u \cdot v}{\|u\| \|v\|} \quad (2)$$

We used an open source python library QuickSOM [29] to construct SOM with a square grid. In the experiment, we tested SOMs of 4 different sizes. They contained 10-by-10, 20-by-20, 30-by-30 or 40-by-40 nodes at square grids. As we did not observe significant dependency on SOMs’ sizes, the analyses below are based on SOMs consisting of 20-by-20 units, unless stated otherwise. Supplemental Table 1 shows the hyperparameters selected for the experiments, and the terminologies are adopted from QuickSom. All neural network models including SOMs were built using Pytorch [30] and tested with a single Nvidia’s RTX 3080 GPU and core i7 CPU.

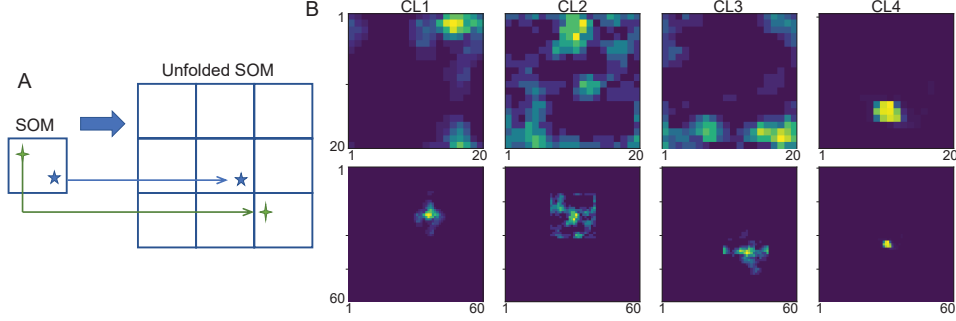


Figure 2: Unfolding SOM. When Euclidean distance between two SOM units or the class centers are estimated, all BMUs are transferred to the unfolded SOM. (A), Torus distance. To estimate the torus distance, all BMUs are mapped onto 9 identical grids. (B), Examples of BMUs in the original (top row) and unfolded (bottom row) SOMs. The columns show BMUs from CL1, CL2, CL3 and CL4, respectively. The class center is the center of mass of BMUs in the unfolded SOMs shown in the bottom row. It should be noted that SOMs in the bottom row are three times larger than the original SOMs in the top row.

2.4 Analysis of functional codes (FCs)

After training, we considered the weights of trained SOMs as effective FCs of ResNets (Fig. 1) and used them to answer two questions. First, can SOMs learn FCs? In other words, can the weights of SOMs mediate semantic meanings of inputs (in our analysis, the labels of inputs)? Second, what properties do FCs in 4 CLs have? To answer the first question, we obtained top-10 BMUs corresponding to individual VCs elicited by images in SOM-tr and SOM-val, and grouped them according to inputs’ labels. If SOMs learn FCs, BMUs corresponding to the VCs elicited by the same class inputs would be close to one another. To answer the second question, we studied BMUs’ relationships to one another by measuring the Euclidean distance (ED) between BMUs and CD (Eq. 2) between their weights.

As a constructed SOM is a torus (due to the periodic boundary condition), we measured the shortest distance between SOMs’ nodes in a torus. Specifically, the trained SOM was mapped onto the center of 9 grids. When we estimated ED between the two SOM units, one of the two units was mapped onto the center grid, and another, onto one of 9 grids (Fig. 2A), in which the shortest distance is available. In our analysis, we also identified the class centers using SOM’s BMUs. In doing so, for each class, we first determined which unit was frequently chosen as BMU while the same class inputs from SOM-tr were fed to ResNet18 and 50. Then, all BMUs of the same class examples were mapped onto one of 9 grids (Fig. 2A), in which the distances to the most frequently chosen BMU were the shortest. The class center is the center of mass of BMUs in this unfolded SOM (see the bottom row of Fig. 2B for examples).

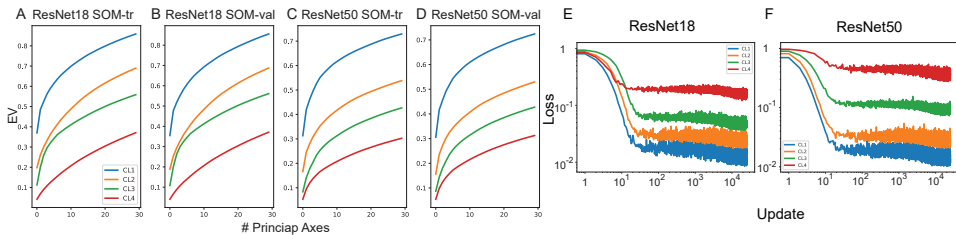


Figure 3: We conduct PCA analyses on VCs from all 4 CLs of ResNet18 and 50. (A), EV measured from ResNet18’ responses (VCs) to SOM-tr (i.e., 50,000 examples from the ImageNet train set). (B), EV measured from ResNet18’ responses (VCs) to SOM-val. (C), EV measured from ResNet50’ responses (VCs) to SOM-tr. (D), EV measured from ResNet50’ responses (VCs) to SOM-val. EVs in CL1, CL2, CL3 and CL4 are shown in blue, orange, green and red, respectively. (E), Loss function of SOMs trained on ResNet18’s CL1, CL2, CL3, CL4 are shown in blue, orange, green and red, respectively. (F), the same as (E) but SOMs are trained on ResNet50’s VCs.

3 Results

The input features are mapped onto hidden representations in DNNs, which in turn are linked to DNNs’ decisions. Given that DNNs can generalize answers on unseen examples, it seems natural to assume that multiple input features

are mapped onto the same representations (or internal codes). If this assumption is valid, the activation patterns can be mapped onto a lower dimensional space. To address this assumption, we perform PCA analysis on VCs from CL1, 2, 3 and 4 of ResNet18/50. Fig. 3A -D show the ratio of explained variance (EV) of top 30 principal axes. As shown in the figures, EV in CL1 increases quite rapidly, as the number of principal axes grows. The growth rate of EV is substantially smaller in deep layers, especially in CL3 and CL4. This result raises the possibility that shallow layers (especially, CL1) could convert diverse input features into homogenous FCs, and deep layers (CL3 and CL4) could convert homogeneous FCs in shallow layers into more diverse FCs. In other words, shallow layers map inputs to a very condensed feature space, and deep layers expand it. This reminds us of telescopes’ operating principles, leading us to our FT hypothesis that ResNets’ shallow and deep layers can function as convex and concave lenses do in the telescope.

3.1 ResNets as Functional Telescopes

To further address this possibility, we seek FCs by training SOMs on VCs from CL1, 2, 3 and 4. To obtain layer-specific FCs, we train 4 individual SOMs on VCs elicited by SOM-tr for 5 epochs. During training, SOMs are updated after accumulating errors over 10 VCs (i.e., the batch size is 10). If all inputs to SOMs are identical, only a single unit would be chosen as BMU, and its weight would approach the input rapidly. If inputs are diverse, more units are chosen as BMUs and learn individual inputs. When a sufficient number of units learn their representations of inputs, SOMs cannot learn new inputs substantially different from previous ones, and thus, the loss function may stay at a relatively high value. Conversely, we could expect the loss function of SOM to reflect the inputs’ diversity. With this possibility in mind, we evaluate the loss function during training. As shown in Fig. 3E, the loss functions of SOMs, trained on ResNet18’s VCs, decline initially and then become saturated at different levels depending on layers. We also observe the equivalent results with the trained ResNet50 (Fig. 3F). These results support our earlier analysis that FCs in shallow layers are homogeneous, but those in deep layers are diverse.

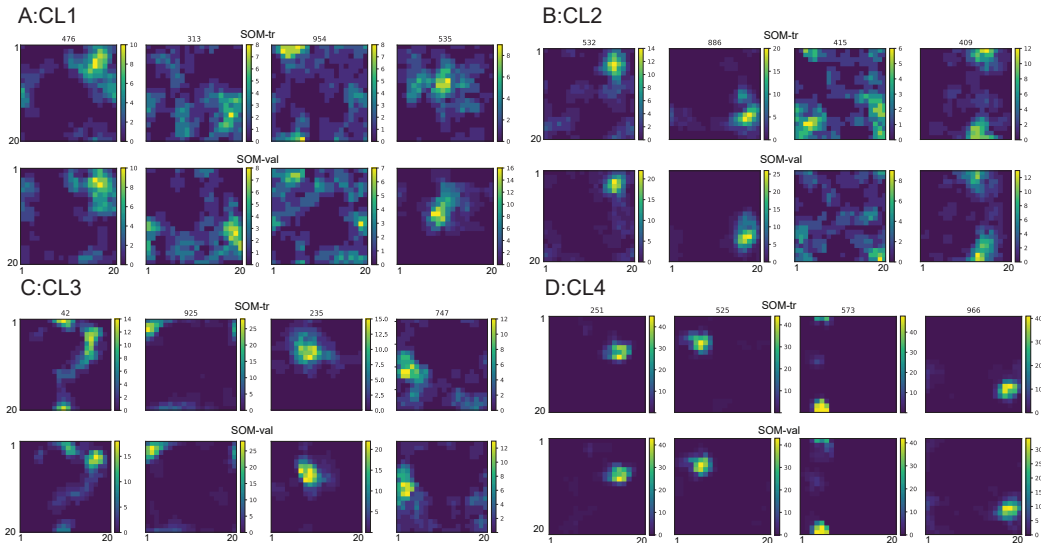


Figure 4: BMUs of VCs of ResNet18. For each input, we collect VCs from CL1-CL4 of ResNet18 and estimate their 10 BMUs in the trained SOM. (A), BMUs in CL1. (B), BMUs in CL2, (C), BMUs in CL3. (D), BMUs in CL4. The top panels show BMUs of examples in SOM-tr, which are used to train SOMs. The bottom panels show BMUs of examples in SOM-val, which are not used to train SOMs. Each column shows BMUs of inputs in the same class; the number above the panels denotes their class id in the ImageNet.

Then, can SOMs learn semantically meaningful codes? If a trained SOM learns FCs essential for ResNets’ operations, its responses to semantically homogeneous inputs could also be homogeneous. That is, BMUs corresponding to such homogeneous inputs can be close to each other or clustered together. Thus, we examine BMUs (SOM’s predictions) of inputs drawn from the same class. As shown in Fig. 4, BMUs of the same class inputs are clustered together. Notably, the spatial spreads of BMUs are relatively bigger in shallow layers but smaller in deep layers. Furthermore, we observe that SOM-val, which is not used to train SOMs, elicits a similar set of units (Fig. 4); we find equivalent results from SOM trained on ResNet50 (Supplemental Fig. 1). These results suggest that SOMs can learn semantically meaningful codes, and their correlations to the labels (i.e., classes) of inputs become stronger in deep layers.

To quantify this observation, we evaluate the Euclidean distance (D_{wc}) between individual BMUs of the same class inputs and their centers. In doing so, we first identify the class center (i.e., the centroids of BMUs of the same class inputs) and calculate the ED in the 2D torus (see section 2.4 and Fig. 2). In this analysis, we calculate the average distances on a class-by-class basis. Fig. 5A and B show the distributions of distances of all 1000 classes. As shown in the figure, the distances to the class centers are much smaller in deep layers than those in shallow layers. The distances measured by unseen examples (from ImageNet validation set) indicate the same trend. We also ask if D_{wc} s are correlated with ResNet’s answers and find that D_{wc} is bigger when ResNet makes an incorrect prediction than when ResNet makes a correct prediction; see supplemental Text and Supplemental Fig. 2.

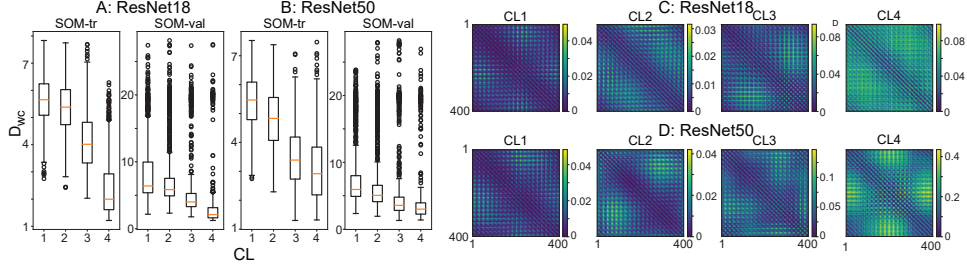


Figure 5: D_{wc} , ED, between individual BMUs to their class centers. For each ImageNet class, we first obtain the class center and calculate the mean distance between BMUs and the class center. To show the statistical properties of all 1000 classes, we use the box plot. (A), D_{wc} measured in ResNet18 using SOM-tr (left) and SOM-val (right). Open circles denote outliers (i.e., classes significantly different from others). We observe outliers more frequently in SOM-val, which is not used to train SOMs. (B), D_{wc} in ResNet50. (C), CD between the weights of SOMs trained on VCs from 4 CLs of ResNet18. (D), CD between weights between SOMs trained on ResNet50. We display all pairs of 400 units in the 20-by-20 SOM.

Our analyses above suggest that SOMs can learn semantically meaningful codes. As SOMs store representative inputs (i.e., FCs in our study) on SOMs’ weights, we further analyze their weights to gain insight into ResNets’ operation. We focus on addressing our FT hypothesis that ResNets can be an effective telescope working on input features. FT hypothesis predicts that FCs in shallow layers are homogeneous, but those in deep layers are diverse. To address this prediction, we first evaluate CDs (Eq. 2) between all weights of SOMs trained on 4 CLs. As shown in Fig. 5 C and D, CDs between weights of SOM trained on CL1 are quite small, but they become bigger when SOMs are trained on deep layers (especially CL4), supporting our FT hypothesis.

We observe that some units are more frequently chosen as BMUs than others and expect them to store more valuable semantic codes. As class center units (nearest neighbors to class centers) represent such units, we examine their similarity to further test our hypothesis. We first identify class center units for 100 random ImageNet classes and estimate CDs between their weights (i.e., proxy of FCs). The CDs between the semantic FCs are the smallest in CL1 and increase in deep layers, which is also consistent with our FT hypothesis (Fig. 6).

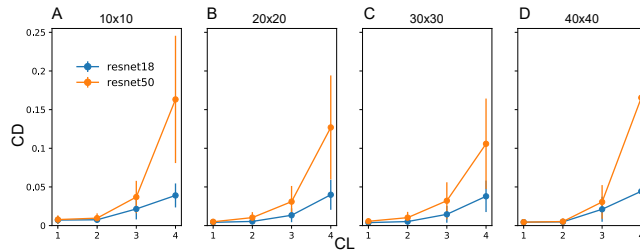


Figure 6: Cosine Distance between class centers’ weights depending on the SOM’s size. (A), CD between 100 class centers in SOM that contains 10-by-10 nodes. x -axis denotes the layer (i.e., CL1-CL4). The blue and orange lines represent ResNet18 and 50, respectively. We display the mean and standard deviations from all pairs of 100 class centers. (B)-(D), the same as (A), but the SOM size is different; see the number above the panels.

3.2 A potential link between FT hypothesis and adversarial perturbations

We note a potential link between our FT hypothesis and DNNs’ generalization ability. If an input feature is mapped onto a condensed space, it would lead to an easier generalization, since unseen examples are in close proximity to

training examples. When data points in shallow layer feature space are closer, they are more likely to be mapped onto the same cluster in deep layers, natively supporting DNNs’ generalization ability. However, this compressed feature space can also make the crosstalk between classes easier, increasing the rate of errors. Conversely, a small perturbation, which can efficiently move data points in this compressed feature space, can easily disrupt ResNets’ decision-making. This possibility may explain DNNs’ vulnerabilities to adversarial perturbations that can effectively change DNNs’ predictions.

To address this possibility, we create adversarial examples and obtain their VCs in all 4 CLs. Specifically, we randomly choose 100 images from ImageNet and perturb them to modify all of DNNs’ answers into ‘toaster’ using projected gradient attack (PGD) [31]; see Supplemental Table 2. The maximal pixel intensity is set to 1, and the maximal magnitude of adversarial perturbations is set to 1/255. 10 images (out of 100) crafted for ResNet18 failed to deceive the model, and 23 images crafted for ResNet50 failed as well. We restrict our analysis to the adversarial images, which can successfully manipulate the ResNet to predict ‘toaster’.

While adversarial inputs are crafted, we estimate the Euclidean distance (Δ_{adv}) between BMUs of normal inputs and BMUs of adversarial inputs and made two observations. First, adversarial inputs have limited influence measured via Δ_{adv} , on CL1, but their impacts on deep layers are much higher in both ResNet18 and in ResNet50 (Fig. 7 A and B). Second, Δ_{adv} in CL1 does not substantially increase over epochs, whereas Δ_{adv} in CL3 and CL4 increase rather continuously. These results suggest that adversarial perturbations do not need to substantially modify FCs in shallow layers to change FCs in deep layers.

Then, how do minimally modified CL1 codes manipulate ResNets’ decisions so effectively? To address this question, we measure the distance (D_{norm}) between normal input’s BMUs and the toaster center and the distance (D_{adv}) between adversarial input’s BMUs and the toaster center. To estimate the toaster center, we feed toaster images from SOM-tr, which are correctly classified as toaster by ResNet18 or 50, and calculate the center of mass of toaster BMUs. During successful attacks, we expect the adversarial input’s BMUs to approach the ‘toaster’ class center. To test if this expectation holds, we estimate D_{ratio} (Eq. 3) during the optimization of adversarial perturbation.

$$D_{ratio} = \frac{D_{adv}}{D_{norm}} = \frac{\sum_{i=1}^{10} \|adv_i - T\|}{\sum_{i=1}^{10} \|norm_i - T\|} \quad (3)$$

, where adv , $norm$ and T represent BMUs of adversarial inputs, BMUs of normal inputs and the toaster center. For each input, we obtain 10 BMUs, and D_{adv} is the average distance over 10 BMUs.

When a BMU moves towards the toaster center, D_{ratio} becomes smaller than 1. Interestingly, the reduction of D_{ratio} becomes apparent only in CL4 (Fig. 7C and D), and D_{ratio} in CL4 declines gradually as the epoch grows. Furthermore, D_{ratio} in CL4 and Δ_{adv} in CL1 are not correlated with one another, suggesting that a stronger perturbation in CL1 does not guarantee a greater success rate in manipulating D_{ratio} in CL4 (Fig. 7C and D).

These observations suggest that FCs in CL1 move rather randomly, whereas those in CL4 move towards the toaster center. Then, how do CL1’s FCs move CL4’s FCs towards the toaster center? It is possible that CL1 has multiple regions, which can be mapped onto the toaster regions in CL4 and are in close proximity to one another. If so, FCs in CL1 could simply move to one of the regions mapped onto the toaster center in CL4. They do not need to move towards CL1’s toaster center to change FCs in CL4 or ResNets’ answers to toaster; see Supplemental Fig. 3 for illustration. Our FT hypothesis predicts that shallow layers have functional regions in condensed space, which can explain our observations.

3.3 Implication for detecting adversarial perturbations

The adversarial perturbations modify hidden layer responses, which could be used to detect adversarial perturbations. Thus, we use FCs identified by SOMs to examine if adversarial inputs can produce detectable traces in ResNets. Specifically, from each input, we obtain 40 BMUs from 4 CLs (top-10 BMUs per a CL) and combine them with ResNets’ predicted class to create an input to an autoencoder, in which 8 linear layers (Fig. 8A) are trained to reconstruct inputs. After training (see Supplemental Table 3 for details), the autoencoder reliably reconstructs the inputs (Fig. 8B). We assume that this model would produce higher reconstruction errors, if adversarial inputs create substantially different FCs in ResNets. As shown in the figure, the reconstruction errors on adversarial FCs are not substantially different from those on normal FCs, suggesting that internal responses to normal and adversarial inputs are almost indistinguishable. This rather surprising result indicates that adversarial perturbations can effectively manipulate ResNets’ answers with minimal manipulation of their internal responses. In fact, this is also consistent with our FT hypothesis suggesting that a small perturbation on CL1 can lead to different semantic FCs in deep layers.

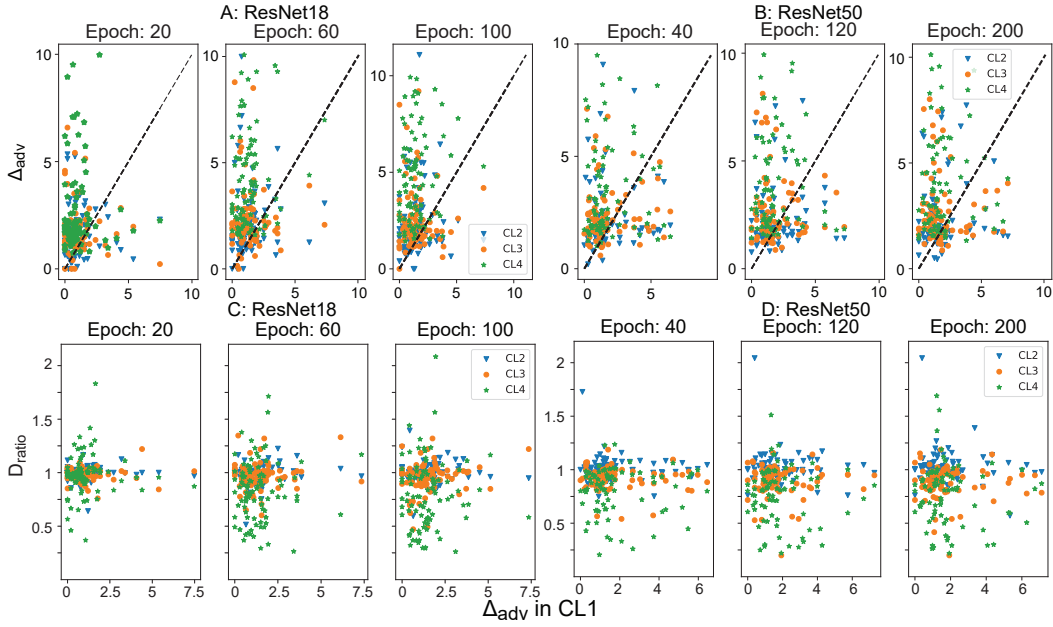


Figure 7: (A), $\Delta_{adv} = \frac{1}{10} \sum_{i=1,10} \|adv_i - norm_i\|$, where adv_i and $norm_i$ represent BMUs of adversarial inputs and BMUs of normal inputs, respectively; that is, Δ_{adv} is the average distance over 10 BMU pairs obtained from a single input. Δ_{adv} in CL2, CL3 and CL4 are shown blue, orange and green, respectively. The intermediate stages of inputs are tested at epochs 20, 60 and 100. The dashed lines denote the reference line, in which $y = x$. (B), the same as (A), but adversarial images are crafted for ResNet50 for 200 epochs. (C), D_{ratio} estimated with adversarial inputs for ResNet18. (D), D_{ratio} for adversarial inputs for ResNet50. For all panels, x -axis denotes the Δ_{adv} in CL1.

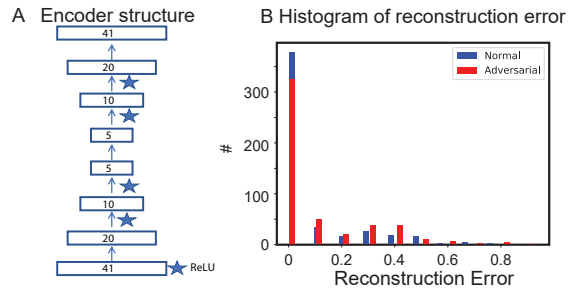


Figure 8: Detecting adversarial perturbation. (A), the diagram of encoder, in which 8 linear layers are used to reconstruct inputs. The rectangles and the number inside them represent fully connected layers and the number of nodes in them. ReLU are marked by the star. (B), histogram of reconstruction errors of normal (blue) and adversarial (red) inputs.

4 Discussion

Based on our results, we propose that DNNs’ operations closely resemble telescopes’ operations. The compressed feature space may be a double-edged sword which produces generalizations readily but creates DNNs vulnerabilities to adversarial perturbations.

4.1 Links to earlier works

Generalization ability is one of DNNs’ key capabilities, and an earlier study suggested that their vulnerabilities to adversarial perturbations are connected to generalization of non-essential features [32]. Our analyses are consistent with their finding and further suggest that such erroneous generalization can easily occur due to compressed feature space. Model stitching [33] suggested that shallow layers from more powerful DNNs can boost less powerful DNNs’ performance. Based on our FT hypothesis suggesting that the essential function of shallow layers is to create condensed feature space, we argue that the shallow layers of better models may compress features into more effective feature space.

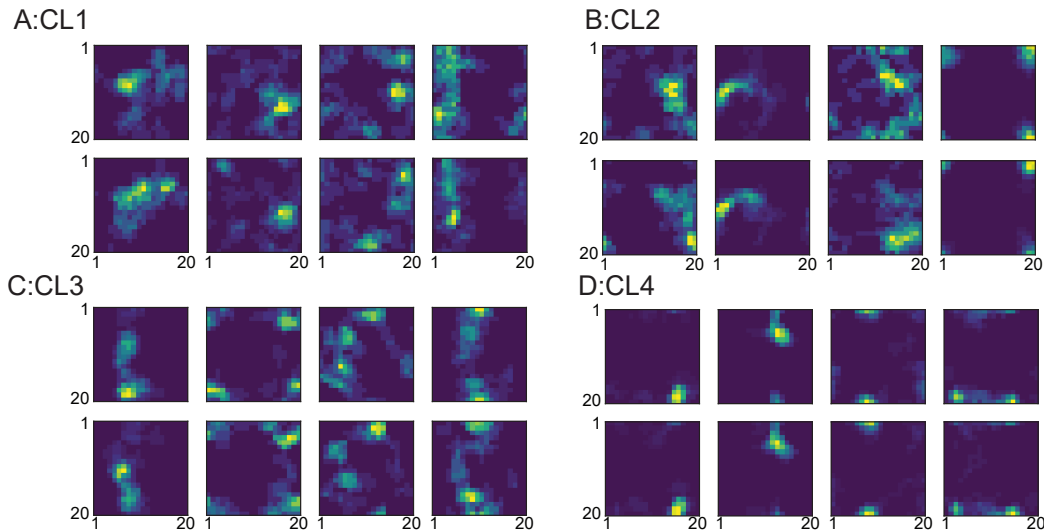
4.2 Limitation and future extension of our analysis

In this study, we analyze ResNets as a representative model architecture of DNNs, as it contain various types of components (e.g., convolution, batch normalization, skip connections) essential for modern DNNs. However, transformers [34] do not rely on convolution but instead rely on attentional heads and fully connected layers. Our results will likely hold for modern convolutional networks, but it remains unclear if our FT hypothesis can explain transformers’ operations. Furthermore, we use a simple coding rule to describe feature maps’ responses, which allows us to analyze ResNet’s internal representations quickly with limited computing resources, but this coding rules may not be powerful enough to fully capture information of feature maps. In the future, we will expand our analysis to non-convolutional architecture such as transformers and recurrent networks and explore optimal coding rules that can efficiently describe feature maps.

Supplemental Material

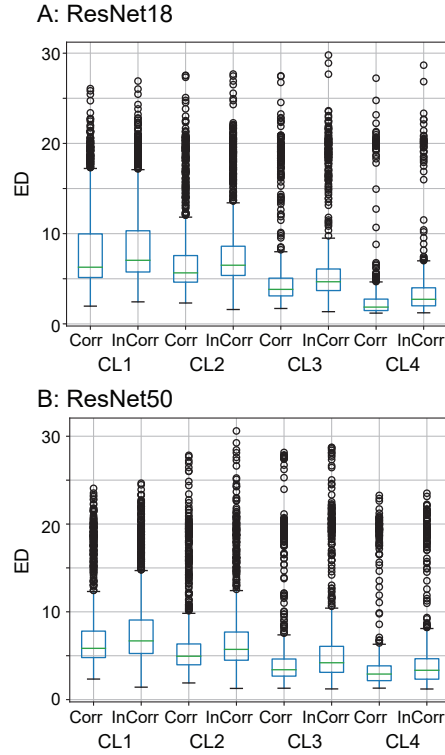
Below, we present Supplemental Figures and Tables.

Supplemental Figures



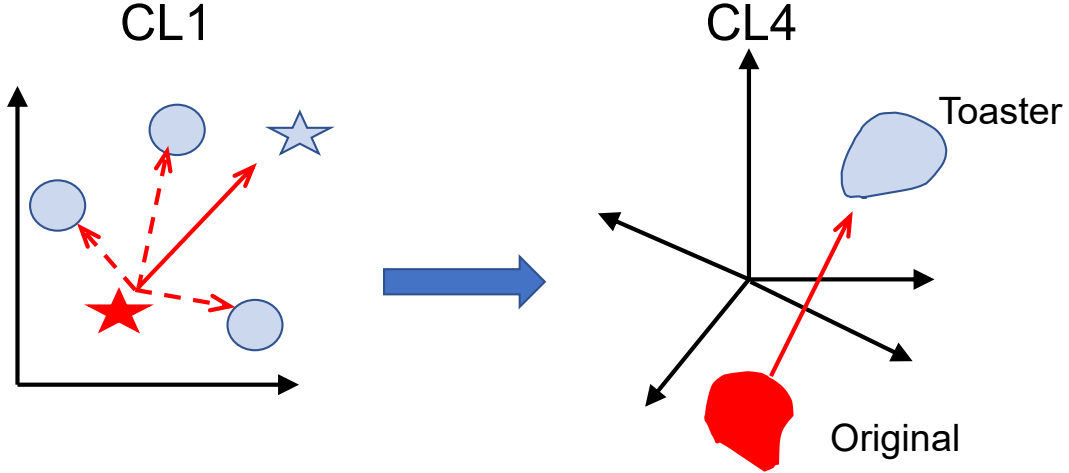
Supplementary Figure 1: BMUs of VCs obtained from ResNet50. The panels show BMUs of SOMs trained on ResNet50. (A), BMUs of VCs in CL1. The top row shows the BMUs of SOM-tr, whereas the bottom row shows the BMUs of SOM-val. Each column shows BMUs of the inputs in the same class. (B), the same as (A), but VCs were obtained from CL2. (C), the same as (A), but VCs were obtained from CL3.(D), the same as (A), but VCs were obtained from CL4.

We test if ResNets utilize FCs for decision-making by estimating the correlations between FCs and ResNets' decisions. In this test, we group FCs depending on whether ResNets make correct predictions of the inputs' labels. If FCs are linked to ResNets' decisions, BMUs storing FCs would be close to the centers of the class predicted by ResNets. If this assumption holds, when ResNets make correct predictions, BMUs storing FCs would be close to the centers of the labels. By contrast, when ResNets make incorrect predictions, they would be close to the centers of the classes different from the labels. Based on this line of thought, we expect the distance (Euclidean distance, ED) between BMUs and the label centers to be bigger when ResNets' make incorrect predictions than when they make incorrect predictions. In the analysis, we estimate the centers of the labels using SOM-tr and test ED between BMUs and the label centers using SOM-val; this is consistent with other analyses, in which the class centers are estimated using SOM-tr only. As shown in Supplemental Fig. 3, ED is bigger on average when ResNets make mistakes.



Supplementary Figure 2: EDs between BMUs and the label centers. For each class, we estimate the mean ED over 50 examples from SOM-val; we consider 10 BMUs per input. The label centers are estimated using SOM-tr. x -axis denotes the data type. EDs are grouped based on CL and whether ResNets make correct predictions (Corr) or not (InCorr). The open circles in the plots denote the outlier classes. (A), EDs measured from SOMs trained on ResNet18. (B), EDs measured from SOMs trained on ResNet50.

Supplemental Tables



Supplementary Figure 3: Illustration of feature maps in CL1 and CL4. The red star represents an original BMU, and the blue star represents the toaster center. The blue ovals denote CL1’s local regions that map onto the toaster region in CL4. The red arrow denotes the direction toward the toaster center. Our analyses suggest that BMUs in CL4 move towards the toaster center, whereas BMUs in CL1 do not. If CL1 has many local regions corresponding to the toaster, BMUs can jump to one of them (dashed arrows) to change FCs in CL4.

Supplementary Table 1: We list the parameters selected for SOM. m and n denote the height and width, respectively. In the experiment, we used a square grid ($m = n$). σ and α denotes their initial values, and they decay over time. We used ‘exp’ decay mode supported by Quicksom [29]

Parameter	value
m (height)	10,20,30,40
n (width)	10,20,30,40
σ	10
α	0.1
decay	exp

Supplementary Table 2: Parameters used to craft adversarial images. We note that it is harder to craft successful attack on ResNet50 and thus used stronger perturbations on ResNet50.

Arguments (name in advertorch)	Value
Loss function (loss_fn)	CrossEntropyLoss(reduction="sum")
Maximum perturbation (eps, ϵ)	$\frac{1}{255}$
Iteration (nb_iter)	100 for ResNet18 and 200 for ResNet50
Update step size (eps_iter)	$\frac{1}{255} \times \frac{2}{100}$ for resnet18 and $\frac{1}{255} \times \frac{6}{100}$ for resnet50
rand_int	True
targeted	True
clip_min	0.0
clip_max	1.0
norm	L_{inf}

Supplementary Table 3: We list the parameters used to train the autoencoder discussed in the main text.

Param	Value
Batch size	20
Learning rate λ ,	0.001
Loss function	Mean Squared Error
Optimizer	Adam
Epoch	30

References

- [1] Yann Lecun, Yoshua Bengio, and Geoffrey Hinton. Deep learning. *Nature*, 521(7553):436–444, 2015.
- [2] Ajay Shrestha and Ausif Mahmood. Review of deep learning algorithms and architectures. *IEEE Access*, 7:53040–53065, 2019.
- [3] Saptarshi Sengupta, Sanchita Basak, Pallabi Saikia, Sayak Paul, Vasilios Tsalavoutis, Frederick Atiah, Vadlamani Ravi, and Alan Peters. A review of deep learning with special emphasis on architectures, applications and recent trends. *Knowledge-Based Systems*, 194:105596, 2020.
- [4] Zachary C. Lipton. The Mythos of Model Interpretability. In *ICML WHI*, 2016.
- [5] Cynthia Rudin. Please Stop Explaining Black Box Models for High Stakes Decisions. In *NIPS Workshop*, 2018.
- [6] Christian Szegedy, Wojciech Zaremba, Ilya Sutskever, Joan Bruna, Dumitru Erhan, Ian Goodfellow, and Rob Fergus. Intriguing properties of neural networks, 2013.
- [7] Anirban Chakraborty, Manaar Alam, Vishal Dey, Anupam Chattopadhyay, and Debdeep Mukhopadhyay. Adversarial attacks and defences: A survey, 2018.
- [8] Xiaoyong Yuan, Pan He, Qile Zhu, and Xiaolin Li. Adversarial examples: Attacks and defenses for deep learning. *IEEE Transactions on Neural Networks and Learning Systems*, 30(9):2805–2824, 2019.
- [9] Chris Olah, Alexander Mordvintsev, and Ludwig Schubert. Feature visualization. *Distill*, 2017. <https://distill.pub/2017/feature-visualization>.
- [10] Matthew D. Zeiler and Rob Fergus. Visualizing and understanding convolutional networks. *CoRR*, abs/1311.2901, 2013.
- [11] Shan Carter, Zan Armstrong, Ludwig Schubert, Ian Johnson, and Chris Olah. Activation atlas. *Distill*, 2019. <https://distill.pub/2019/activation-atlas>.
- [12] Bruno Olshausen and David Field. Emergence of simple-cell receptive field properties by learning a sparse code for natural images. *Nature*, 381:607–9, 07 1996.
- [13] Ramprasaath R. Selvaraju, Michael Cogswell, Abhishek Das, Ramakrishna Vedantam, Devi Parikh, and Dhruv Batra. Grad-CAM: Visual explanations from deep networks via gradient-based localization. *International Journal of Computer Vision*, 128(2):336–359, oct 2019.
- [14] Mukund Sundararajan, Ankur Taly, and Qiqi Yan. Axiomatic attribution for deep networks. In Doina Precup and Yee Whye Teh, editors, *Proceedings of the 34th International Conference on Machine Learning*, volume 70 of *Proceedings of Machine Learning Research*, pages 3319–3328. PMLR, 06–11 Aug 2017.
- [15] Marco Ancona, Enea Ceolini, Cengiz Öztireli, and Markus Gross. Towards better understanding of gradient-based attribution methods for deep neural networks. In *International Conference on Learning Representations*, 2018.
- [16] Grégoire Montavon, Alexander Binder, Sebastian Lapuschkin, Wojciech Samek, and Klaus-Robert Müller. *Layer-Wise Relevance Propagation: An Overview*, pages 193–209. Springer International Publishing, Cham, 2019.
- [17] Chris Olah, Alexander Mordvintsev, and Ludwig Schubert. Feature visualization. *Distill*, 2017. <https://distill.pub/2017/feature-visualization>.
- [18] Been Kim, Martin Wattenberg, Justin Gilmer, Carrie Cai, James Wexler, Fernanda Viegas, and Rory sayres. Interpretability beyond feature attribution: Quantitative testing with concept activation vectors (TCAV). In Jennifer Dy and Andreas Krause, editors, *Proceedings of the 35th International Conference on Machine Learning*, volume 80 of *Proceedings of Machine Learning Research*, pages 2668–2677. PMLR, 10–15 Jul 2018.
- [19] Guillaume Alain and Yoshua Bengio. Understanding intermediate layers using linear classifier probes, 2018.
- [20] Jung Hoon Lee. Library network, a possible path to explainable neural networks, 2019.
- [21] T. Kohonen. The self-organizing map. *Proceedings of the IEEE*, 78(9):1464–1480, 1990.
- [22] T. Kohonen and T. Honkela. Kohonen network. *Scholarpedia*, 2(1):1568, 2007. revision #127841.
- [23] Archit Rathore, Nithin Chalapathi, Sourabh Palande, and Bei Wang. Topoact: Visually exploring the shape of activations in deep learning, 2021.
- [24] Emilie Purvine, Davis Brown, Brett Jefferson, Cliff Joslyn, Brenda Praggastis, Archit Rathore, Madelyn Shapiro, Bei Wang, and Youjia Zhou. Experimental observations of the topology of convolutional neural network activations, 2022.

- [25] Guillaume Alain and Yoshua Bengio. Understanding intermediate layers using linear classifier probes. *arXiv*, 2016.
- [26] Kaiming He, Xiangyu Zhang, Shaoqing Ren, and Jian Sun. Deep residual learning for image recognition, 2015.
- [27] Ross Wightman. Pytorch image models. <https://github.com/rwightman/pytorch-image-models>, 2019.
- [28] Jia Deng, Wei Dong, Richard Socher, Li-Jia Li, Kai Li, and Li Fei-Fei. Imagenet: A large-scale hierarchical image database. In *2009 IEEE conference on computer vision and pattern recognition*, pages 248–255. Ieee, 2009.
- [29] Vincent Mallet, Michael Nilges, and Guillaume Bouvier. quicksom: Self-Organizing Maps on GPUs for clustering of molecular dynamics trajectories. *Bioinformatics*, 37(14):2064–2065, 11 2020.
- [30] Adam Paszke, Sam Gross, Soumith Chintala, Edward Chanan, Gregory Yang, Zachary DeVito, Alban Lin, Zeming Desmaison, Luca Antiga, and Adam Lerer. Automatic differentiation in PyTorch. In *NIPS Autodiff Workshop*, 2017.
- [31] Aleksander Madry, Aleksandar Makelov, Ludwig Schmidt, Dimitris Tsipras, and Adrian Vladu. Towards deep learning models resistant to adversarial attacks, 2017.
- [32] Andrew Ilyas, Shibani Santurkar, Dimitris Tsipras, Logan Engstrom, Brandon Tran, and Aleksander Madry. Adversarial examples are not bugs, they are features. In H. Wallach, H. Larochelle, A. Beygelzimer, F. d'Alché-Buc, E. Fox, and R. Garnett, editors, *Advances in Neural Information Processing Systems*, volume 32. Curran Associates, Inc., 2019.
- [33] Yamini Bansal, Preetum Nakkiran, and Boaz Barak. Revisiting model stitching to compare neural representations. In A. Beygelzimer, Y. Dauphin, P. Liang, and J. Wortman Vaughan, editors, *Advances in Neural Information Processing Systems*, 2021.
- [34] Jacob Devlin, Ming-Wei Chang, Kenton Lee, and Kristina Toutanova. BERT: pre-training of deep bidirectional transformers for language understanding. In Jill Burstein, Christy Doran, and Thamar Solorio, editors, *Proceedings of the 2019 Conference of the North American Chapter of the Association for Computational Linguistics: Human Language Technologies, NAACL-HLT 2019, Minneapolis, MN, USA, June 2-7, 2019, Volume 1 (Long and Short Papers)*, pages 4171–4186. Association for Computational Linguistics, 2019.